Journal of Materials Chemistry A

PAPER

View Article Online
View Journal | View Issue

Cite this: J. Mater. Chem. A, 2017, 5, 17998

Design and construction of a ferrocene based inclined polycatenated Co-MOF for supercapacitor and dye adsorption applications†

Richa Rajak,[a] Mohit Saraf,[b] Akbar Mohammad[a] and Shaikh M. Mobin *[abc]

A new cobalt based inclined polycatenated metal–organic framework, $\{[Co_4(FcDCA)_4(bpy)_4(H_2O)_6]\cdot 11H_2O\}_n$ [FcDCA = 1,1′-ferrocene dicarboxylic acid and bpy = 4,4′-bipyridyl] (**1**), has been designed and synthesized in a facile manner. **1** can be simplified as a 2D + 2D → 3D inclined polycatenation class with Doc1/1, as authenticated by single crystal X-ray studies. Further, **1** was employed as a modifier for a glassy carbon electrode (**1-GCE**) without using any binders to explore its supercapacitor performance. Detailed electrochemical investigations carried out using **1-GCE** reveal a specific capacitance of 446.8 F g^{-1} at a current density of 1.2 A g^{-1}, with an excellent cycle life of ~88.37% (after 800 cycles). Moreover, a high rate performance was also observed for **1-GCE** (it retains 81% of its initial capacitance up to a high current density of 10 A g^{-1}), which endorsed its good stability on the electrode surface. The results were found to be superior than those for $\{[Co(bpy)_{1.5}(NO_3)_2]\}_n$ (**2**), highlighting the role of the presence of FcDCA in **1**. Additionally, the notable adsorption and desorption properties of **1** towards selected Chicago Sky Blue (CSB) and Congo Red (CR) dyes confirms the candidature of **1** as a potential dye adsorbing agent.

Received 2nd May 2017
Accepted 14th July 2017

DOI: 10.1039/c7ta03773b

rsc.li/materials-a

Introduction

Owing to their fascinating structures and tunable magnetic[15] and optical[16] properties, metal–organic frameworks (MOFs) have potential applications including gas storage,[1–3] catalysis,[4–7] sensors,[8–11] solar cells,[12] Li-ion batteries,[13,14] and so on. Due to the growing demand for energy, the long-time storage of energy has become a challenging task. In this regard, the focus is on the development of new generation supercapacitors as one type of energy storage system with high power density, long cycle life and excellent reversibility.[17,18] Very recently, MOF based materials have also been engaged as supercapacitors for vital energy storage devices.[19,20] It is to be noted that MOFs are also used as single-source molecular precursors for the synthesis of metal oxides,[21] metal hydroxides,[22] porous carbon[23,24] and mixed-metal oxides,[25] *etc.* for their application in supercapacitor studies. On the other hand, considerable attention has been geared towards employing pristine MOFs directly as an active electrode material for supercapacitor applications.[26–29] The performance of supercapacitors engaging nanomaterials or nanocomposites as electrode materials has been well documented.[26,30–32] However, pristine MOF based electrode materials for supercapacitance studies are still rare.[33,34] Among the studied MOFs, the following are widely used: (i) layered MOFs,[15,20] (ii) 3D-porous networks[34] and (iii) mesoporous and 2D-sheet like MOFs[28] with good to excellent specific capacitance.[35] However, only one report is available on polycatenated entangled MOFs of Zn and Cd with very low specific capacitances of 23 F g^{-1} and 22 F g^{-1}, respectively.[36]

In spite of the energy storage applications, there is also rapidly growing concern about water treatment, as the usage of organic dyes has increased over time in essential industrial products such as pharmaceuticals, leather, paper, food, linen, silk, cotton and fiber. Dyes with neutral, positively and negatively charged properties are typically difficult to degrade due to their stability under light and oxidation.[37–41] Hence, the removal of dyes before wastewater is discharged into nature is imperative. Traditional absorption techniques based on zeolites, polymeric materials and activated carbons, as well as chemical degradation and membrane filtration technologies, have been well documented.[37] However, these methods are incomparable with the highly effective, selective and low cost ion exchange processes using ionic and porous MOFs. In recent years, MOFs have been applied in the field of selective adsorption and separation of dyes.[37–41] The incorporation of MOFs as dye adsorbing agents has become a compelling approach to remove hazardous contaminants from both liquid and vapour phases.

[a]Discipline of Chemistry, Indian Institute of Technology Indore, Simrol, Khandwa Road, Indore 453552, India. E-mail: xray@iiti.ac.in; Tel: +91 731 2438 762

[b]Discipline of Metallurgy Engineering and Materials Science (MEMS), Indian Institute of Technology Indore, Simrol, Khandwa Road, Indore 453552, India

[c]Centre of Biosciences and Biomedical Engineering, Indian Institute of Technology Indore, Simrol, Khandwa Road, Indore 453552, India

† Electronic supplementary information (ESI) available. CCDC 1534717 and 1543603. For ESI and crystallographic data in CIF or other electronic format see DOI: 10.1039/c7ta03773b

However, their applicability as effective toxic dye removal species is yet to be explored.

Due to their fascinating properties, topological features and intricate molecular architectures, various entangled MOFs such as (poly)catenanes, (poly)rotaxanes and polythreaded MOFs have been proposed. In a polycatenation network the whole entangled array has a higher dimensionality than each of the component motifs, and each individual component is entangled only with the surrounding ones but not with all the others.[10] In general, various carboxylate linkers such as trimesic acid (benzene-1,3,5-tricarboxylic acid) and terephthalic acid (benzene-1,4-dicarboxylic acid) have been actively engaged in the formation of such entangled MOFs,[11,47] but to the best of our knowledge, so far no report is available on using organometallic based 1,1′-ferrocenedicarboxylic acid (FcDCA) as a linker for constructing polycatenated MOFs. The presence of ferrocene, a highly electroactive species, may lead to metal-rich entangled MOFs for superior supercapacitor and dye adsorption performances than those reported so far for any polycatenated MOFs. In addition, FcDCA is an excellent candidate since it contains a stable ferrocene moiety and has more coordination donors, so it can possibly induce a variety of coordination modes.[48a] Moreover, the introduction of various pyridyl linkers, along with carboxylate ligands, may introduce structural flexibility into the whole framework. Hence, a mixed ligand strategy to construct inclined polycatenated MOFs could offer new possibilities by providing flexibility and stability to the whole framework.[38–47]

With the above aspects in mind, we have designed a new inclined polycatenated Co-MOF, $\{[Co_4(FcDCA)_4(bpy)_4(H_2O)_6]\cdot 11H_2O\}_n$ (**1**), by a facile mixed ligand approach employing 1,1′-ferrocene dicarboxylic acid (H_2FcDCA) and 4,4′-bipyridyl (bpy). We have also synthesized $\{[Co(bpy)_{1.5}(NO_3)_2]\}_n$ (**2**) under stirring conditions at room temperature for the purpose of comparison and to study the effects of the presence of FcDCA. To the best of our knowledge, we report for the first time a FcDCA based inclined polycatenated Co-MOF (**1**) for energy storage applications. Additionally, the dye adsorption abilities of **1** and **2** were also examined for two different dyes containing azo groups (Chicago Sky Blue: CSB and Congo Red: CR).

Experimental

Materials

All materials were procured from Merck and used in the experiments as received. The solvents were used without any further purification.

Instruments

Single-crystal X-ray structural studies were conducted on a Rigaku-Oxford Supernova CCD diffractometer equipped with a low-temperature attachment. Powder X-ray diffraction (PXRD) data was recorded on a Rigaku Smart Lab X-ray diffractometer using monochromated Cu-Kα radiation (0.154 nm). Thermogravimetric analysis (TGA) was performed on a METTLER TOLEDO (TGA/DSC 1) system using the STAR^e software system up to 800 °C under N_2 flow with a heating rate of 10 °C min^{-1}. IR spectra (4000–400 cm^{-1}) were recorded using a KBr pressed pellet on a Bio-Rad FTS 3000MX instrument. Surface morphology was obtained using a Supra 55 Zeiss field emission scanning electron microscope (FESEM). The N_2 adsorption–desorption isotherm was measured on an Autosorb iQ, version 1.11 (Quantachrome Instruments). UV-visible analysis was conducted on a Varian Cary 100 Bio UV-Visible Spectrophotometer. Conductivity measurements of **1** and **2** were performed using a Wayne Kerr Impedance Analyzer (LCR Meter), 6500B.

Electrochemical measurements

The electrochemical analyses were carried out on a computer controlled electrochemical workstation (Autolab PGSTAT 204N using NOVA software; version 1.10). A standard three electrode configuration involving platinum wire as the counter electrode, Ag/AgCl as the reference electrode, and a 3 mm diameter glassy carbon electrode (GCE) as the working electrode was incorporated. All measurements were conducted at room temperature (RT).

Crystallographic data collection and structure determination

The single crystals of compounds **1** and **2** were mounted on a Rigaku-Oxford Supernova CCD Diffractometer and the Single Crystal X-ray data were collected at RT (293 K) using graphite-monochromated Cu-Kα ($\lambda\alpha$ = 1.54814 Å). The data collections were evaluated using the CrysAlisPro CCD software. The data were collected by standard φ–ω scan techniques and scaled as well as reduced by the CrysAlisPro RED software. The crystal structures were solved by direct methods using SHELXS-97 and refined by full-matrix least squares with SHELXL-97 on F^2.[49] The positions of all of the atoms were obtained by direct methods. All non-H atoms were refined anisotropically. All the H atoms were placed in geometrically constrained positions and refined with isotropic temperature factors, generally 1.2 ThU_{eq} of their parent atoms. The potential solvent accessible volume of **1** was calculated using PLATON. The solvent molecules of **2** were removed by the SQUEEZE[50] program and a new HKL file was generated. The structure was solved using the newly generated HKL file. The hydrogen-bonding interactions, molecular drawings and mean-plane analyses were obtained using the Diamond program (ver. 3.1d).[49] The crystal and refinement data are summarized in Table 1, and selected bond distances and angles are shown in Table S1 in the ESI.† Despite several attempts, we could not generate better quality single crystals of **1**.

Synthesis of 1

An aqueous solution (10 mL) of the sodium salt of H_2FcDCA (0.2 mmol, 54 mg) was mixed with a methanolic solution (10 mL) of 4,4′-bipyridyl (0.2 mmol, 31 mg) and the resulting solution was stirred for 1 h to achieve a clear solution. Parallel to this, an aqueous solution (10 mL) of $Co(NO_3)_2\cdot 6H_2O$ (0.2 mmol, 58 mg) was prepared. Finally, 2 mL of the above mixed ligand solution was gradually and carefully layered above 2 mL of the aqueous $Co(NO_3)_2\cdot 6H_2O$ solution in a narrow glass tube using 2 mL of buffer (1 : 1 H_2O and MeOH) solution. Orange-red colored block-shaped crystals were obtained after one week

Table 1 Crystal data and structure refinement for **1** and **2**

Identification code	**1**	**2**
Empirical formula	$C_{88}H_{98}Co_4Fe_4N_8O_{33}$	$C_{15}H_{12}CoN_5O_6$
Formula weight	2254.86	417.23
Crystal system	Orthorhombic	Orthorhombic
Space group	$P2_12_12_1$	*Fddd*
a (Å)	16.0270(6)	11.38150(10)
b (Å)	18.4421(7)	20.5728(5)
c (Å)	32.2078(17)	34.5573(5)
α (deg)	90	90
β (deg)	90	90
γ (deg)	90	90
V (Å^3)	9519.7(7)	8091.6(2)
Z, d_{calcd} (mg m^{-3})	4, 1.573	16
Temperature (K)	293(2)	293(2)
θ range (deg)	3.644 to 71.232	4.621 to 71.359
Goodness-of-fit	0.965	1.104
R_1, wR_2 [$I > 2\sigma(I)$]	$R_1 = 0.1322$, w$R_2 = 0.2743$	$R_1 = 0.0463$, w$R_2 = 0.1393$
R_1, wR_2 (all data)	$R_1 = 0.3072$, w$R_2 = 0.3831$	$R_1 = 0.0549$, w$R_2 = 0.1472$
F(000)	4632	3392
Crystal size (mm^3)	0.230 × 0.180 × 0.130	0.300 × 0.250 × 0.190
μ (mm^{-1})	10.798	7.009
Index ranges	$-19 \le h \le 17$, $-18 \le k \le 22$, $-39 \le l \le 39$	$-9 \le h \le 13$, $-24 \le k \le 25$, $-40 \le l \le 42$
Absorption correction	Semi-empirical from equivalents	Semi-empirical from equivalents
Max. and min. transmission	1.00000 and 0.23648	1.00000 and 0.55642
Refinement method	Full-matrix least-squares on F^2	Full-matrix least-squares on F^2
Data/restraints/parameters	18 172/31/1213	1971/0/124
Largest diff. peak and hole (e Å^{-3})	1.245 and −0.529	0.285 and −0.388
CCDC no.	1534717	1543603

from the junction of the layers. The crystals were separated, collected and washed with MeOH and subsequently air-dried (yield: 68 mg; 0.03 mmol: ~60%). FT-IR (KBr pellet, cm^{-1}): 3395.04 (b), 1733.82 (w), 1610.34 (m), 1534.66 (m), 1470.95 (s), 1384.28 (s), 1212.35 (w), 1042.66 (w), 807.35 (w), 631.27 (w). The powder form of the bulk compound was prepared by direct mixing of the ligand mixture solution with a corresponding solution of $Co(NO_3)_2 \cdot 6H_2O$, followed by overnight stirring.

Synthesis of 2

The synthesis of **2** was carried out using previously reported methods with certain modifications.[51–54] A methanolic solution of $Co(NO_3)_2 \cdot 6H_2O$ (0.2 mmol, 58 mg) and bpy (0.6 mmol, 93 mg) was stirred for 1 h at RT (dark-pink colored). The obtained product was filtered to remove the unreacted materials. The filtrate was allowed to crystallize at RT. The dark-pink block shaped single crystals of **2** were obtained by slow evaporation of the solvent within 2 days (yield: 60 mg; 0.14 mmol: ~73%). FT-IR (KBr pellet, cm^{-1}): 3423.22 (b), 3046.90 (w), 1608.48 (s), 1478.33 (m), 1305.13 (s), 1221.17 (w), 1070.21 (m), 1012.19 (m), 812.95 (s), 733.22 (w), 632.26 (m).

Electrode fabrication

The supercapacitor tests were performed using glassy carbon electrodes (GCEs). Three GCEs were cleaned by polishing with alumina slurries and subsequently rinsed with DI water, followed by drying. Thereafter, 5 mg of **1** was dispersed in 10 mL of ethanol using ultra-sonication for half an hour. 5 μL of this dispersion (~2.5 μg mass loading) was found to be optimum and was drop-casted onto one of the GCEs and air dried. Finally, the as-formed modified GCE was rinsed with DI water and again dried before it was assembled into an electrochemical workstation. The thus-fabricated electrode was denoted **1-GCE**. Similarly, **2-GCE** was also fabricated.

Dye adsorption study

The dye adsorption study was performed by monitoring the adsorption of dyes in the aqueous phase. In a typical experiment, 22 mg of the selected Chicago Sky Blue (CSB) and Congo Red (CR) dyes were dissolved in 1 L DI water, and 40 mL of the as-formed solutions were taken out for the study. **1** was added to these dye solutions (3 mg/4 mL) and stirred continuously at RT. Thereafter, 3 mL of the dye suspensions were withdrawn at a regular time interval and centrifuged. The UV-vis spectra of the supernatant solutions were recorded to monitor the characteristic absorption peaks of each dye. Additionally, an adsorption study of **2** towards CSB and CR was also performed. However, we noticed the partially soluble nature of **2** in water (which was also the medium of our study).

The recyclability of **1** towards CSB and CR was studied by performing the adsorption experiment thrice for each dye under similar reaction conditions. For the recycling experiment, **CSB@1** or **CR@1** was left for 48 h to achieve the maximum desorption of the dye in the solution. Afterwards, the adsorbent **1** was separated by centrifugation and washed repeatedly with a water and ethanol solution. Finally, the recovered **1** was air dried for further use.

Results and discussion

Orange-red colored crystals of **1** were obtained by mixing an aqueous solution of $Co(NO_3)_2 \cdot 6H_2O$ with the mixed ligands 4,4′-bipyridyl (bpy) and 1,1′-ferrocene dicarboxylic acid (FcDCA) in aqueous methanolic solution by a simple slow diffusion technique at RT (Scheme 1). In general, polycatenated MOFs are constructed at high temperature,[55–57] however, the present work deals with a simple slow diffusion technique at RT in a facile manner.[58,59]

1 and **2** were characterized by various techniques such as PXRD, TGA, FT-IR, SEM and BET, and their crystal structures were authenticated by SCXRD. The PXRD spectra of the bulk compounds (**1** and **2**) agree well with the simulated XRD spectra generated from the single-crystal X-ray data, indicating the structural identities as well as the phase purities of the bulk compounds (Fig. S1 and S2†). The TGA profile of **1** shows a weight loss of ~13% (calcd ~13.57%) in the temperature range of 80–115 °C, which can be assigned to the weight loss of 11 lattice water molecules and six coordinated water molecules from the framework, which is further stable up to 191 °C. Further, the temperature weight loss occurs due to decomposition of the organic ligands (Fig. S3†). While the TGA spectrum of **2** was almost stable up to 212 °C, afterwards loss occurred due to decomposition of the organic moiety (Fig. S4†). The vibrational frequencies of **1** appear in the range of 3400–3200 cm^{-1} in the IR spectrum and correspond to coordinated/uncoordinated water molecules. The other important IR frequencies of **1** are $\nu_{C=N}$ = 1534 cm^{-1}, $\nu_{C=O}$ = 1610 cm^{-1}, $\nu_{C=C}$ = 1470 cm^{-1}, ν_{Co-O} = 807 cm^{-1} and ν_{Co-N} = 631 cm^{-1} (Fig. S5†).

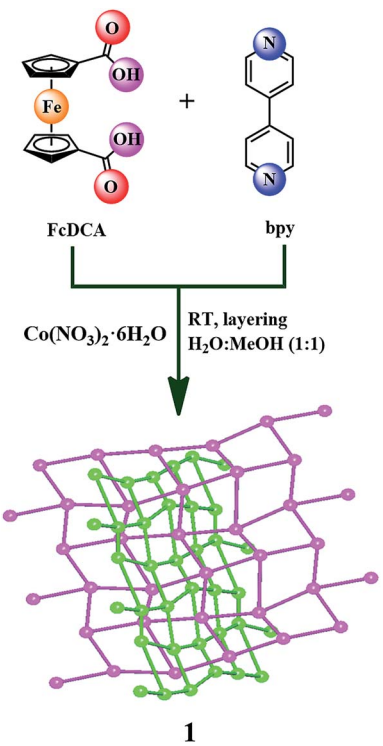

Scheme 1 Schematic representation of the synthesis of **1**.

The vibrational frequencies of **2** correspond to the coordinated NO_3 groups in the IR spectrum and appear in the range of 1600–1000 cm^{-1}, and aromatic C=N appears at nearly 1608 cm^{-1}. Co–N can be assigned to 632 cm^{-1} (Fig. S6†). The morphologies of **1** and **2** were obtained through SEM analysis. The obtained results show that **1** and **2** have block shaped morphologies with an average diameter in the range of ~0.8 μm and 1.2–1.4 μm, respectively. However, some aggregates of **1** and **2** were also observed (Fig. S7 and S8†).

Crystal structure of 1

1 crystallizes in an orthorhombic system with the $P2_12_12_1$ space group. The asymmetric unit of **1** contains four Co(II) centres, four $FcDCA^{2-}$ ligands, four bpy linkers and six coordinated water molecules, along with eleven lattice water molecules (Fig. S9†). The Co1(II) and Co4(II) ions are coordinated with two N atoms from the two bpy ligands, two O atoms of two monodentate $FcDCA^{2-}$ ligands and two O atoms of the coordinated water molecules. In contrast, the Co2(II) and Co3(II) ions are coordinated *via* three O atoms of two $FcDCA^{2-}$, two N atoms from the two bpy ligands and one O atom of the coordinated water molecule, as shown in Fig. 1a. It has been observed that around each Co(II) centre, the coordinated O atoms are in the equatorial positions, whereas the N atoms are located in the axial positions (Fig. S10†), which leads to a distorted octahedral geometry around each Co(II) centre. Each bpy ligand is linked to two Co(II) centres in a trans fashion (N1–Co1–N6 = 178.11°, N3–Co2–N2 = 176.01°, N7–Co3–N5 = 178.13° and N4–Co4–N8 = 170.94°) with a Co(II)–Co(II) separation in the range of 11.4151(4) Å to 11.4541(4) Å. The measured bond distances of Co–O are in the range of 1.994–2.187 Å, and the Co–N bond lengths are in the range of 2.114–2.19 Å. In **1**, the two pyridine rings of the bpy linkers are twisted about ~23°, ~42°, ~41°, and ~17° to each other (Chart 1). Each $FcDCA^{2-}$ ligand coordinates to two Co(II) centres in both a monodentate and a bidentate fashion through the $-COO^-$ group. Two nearby Co1(II)/Co4(II) centres are connected through monodentate carboxylate groups of $FcDCA^{2-}$ ligands and generate a 1D layer of $[Co(FcDCA)]_n$, where the Co1(II)–Co1(II) separation is 9.755(8) Å. In contrast, in the neighbouring 1D Chain, the $FcDCA^{2-}$ ligand is linked to two Co(II) centres alternately *via* a bidentate and a monodentate mode, with a separation between the Co2(II)–Co3(II) centres of 8.343(7) Å and 11.176(7) Å, respectively, as shown in Fig. S11† & Chart 1. Further, these two neighbouring 1D layers are connected to each other by bridging bpy ligands, forming a 2D-network along the *c* axis (Fig. 1b and S12†). Additionally, other similar 2D-networks were found to intercalate each other and form a 3D-framework. However, this 3D-metal organic framework is connected by H-bonding interactions through the lattice water molecules between the free oxygen of the $-COO^-$ group of the FcDCA ligand and the coordinated water molecules. The π···π and C–H···π interactions result in structural integrity to stabilize the MOF (Fig. S13†).

Closer observation of the packing and topological features reveals two sets of parallel sql layers that are polycatenated in an inclined way, followed by the interpenetration of two adjacent

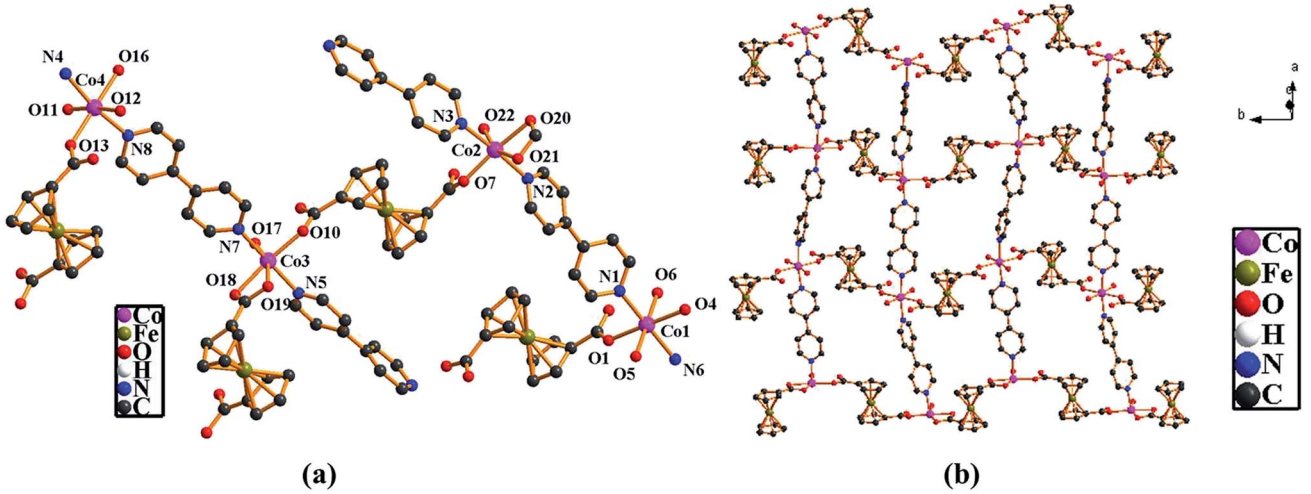

Fig. 1 Ball-stick model showing the (a) coordination environment around the Co(II) ion centre in **1** and (b) 2D framework of **1** along the *c*-axis. Color code: Co (magenta), Fe (olive), O (red), H (white), N (blue), and C (dark gray) (lattice water molecules have been omitted for clarity).

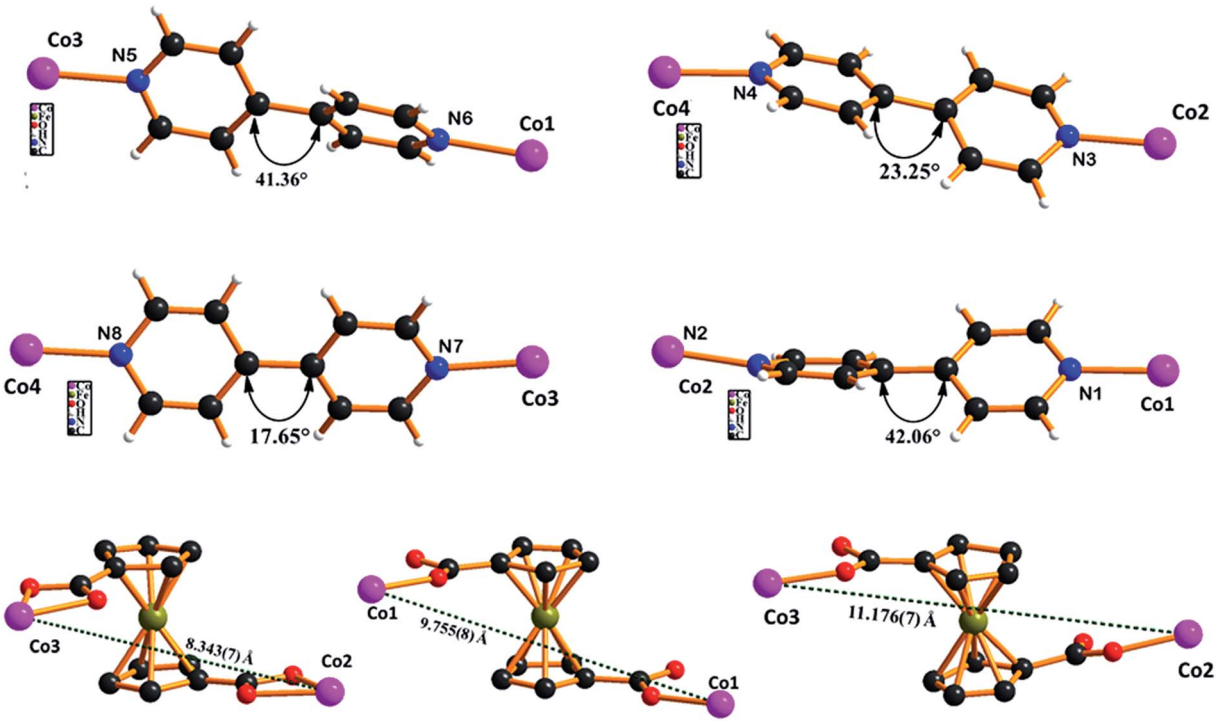

Chart 1 Orientation of the pyridine groups in the bpy linker and various binding modes of the FCDCA ligand found in **1**.

single layers (Fig. 2a), resulting in the formation of a 2D + 2D → 3D inclined polycatenation class with a Doc1/1 framework. The orientations of group 1 and group 2 are [1, 0, −2] and [1, 0, 2], respectively; the inclination angle of groups 1 and 2 is 89.7° (Fig. 2b and c). The total solvent-accessible volume of **1** was estimated to be 1640 Å^3, which is 17.24% of the total crystal volume (9519.71 Å^3). The 3D framework is stabilized by intra/inter-molecular hydrogen-bonding, π···π, and C–H···π interactions (Table S2†).

Crystal structure of 2

2 crystallizes in an orthorhombic system with the *Fddd* space group. Each Co(II) ion of **2** contains CoO_4N_3 with a distorted pentagonal bipyramidal geometry comprising two axial and one equatorial N atoms from three 4,4′-bpy ligands and four equatorial O atoms occupied by two bidentate nitrate ions (Fig. 3a & S14†). Each Co(II) ion centre acts as a T-shaped building unit, leading to a 1D non-interpenetrating ladder type framework along the *b*-axis, as shown in Fig. 3b. The structural analysis of **2** reveals 1D infinite ladders that are juxtaposed in the *ac* plane.

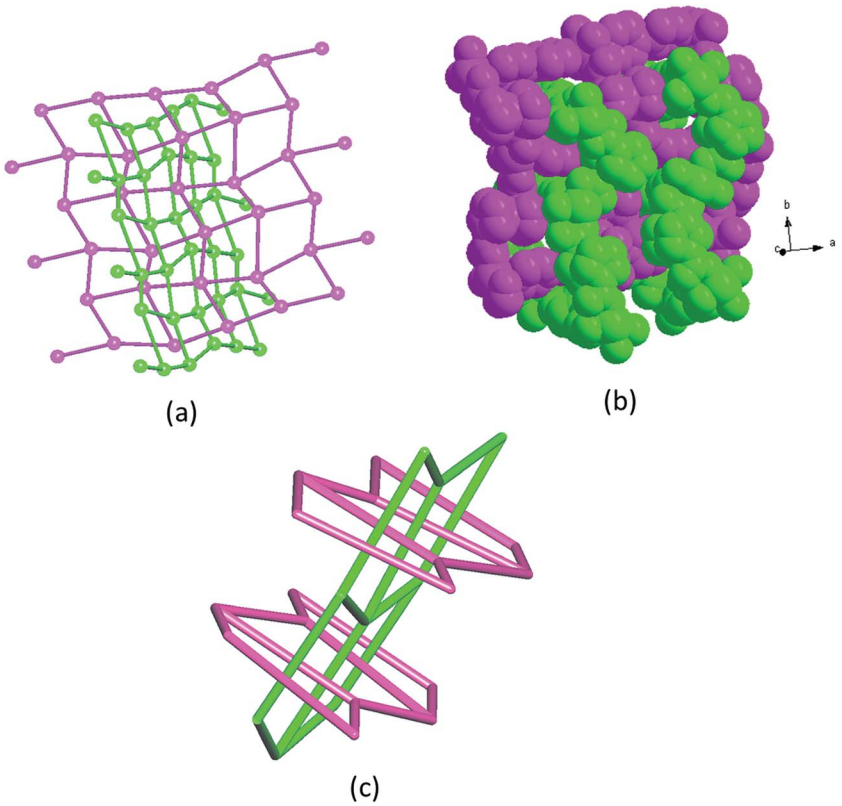

Fig. 2 (a) A representation of the interpenetration of two adjacent single sql layers, (b) a space filling model of the 2D + 2D → 3D inclined polycatenated framework along the *c*-axis, and (c) a simplified topological demonstration of the 2D + 2D → 3D inclined polycatenation of two sets of parallel sql layers in **1**.

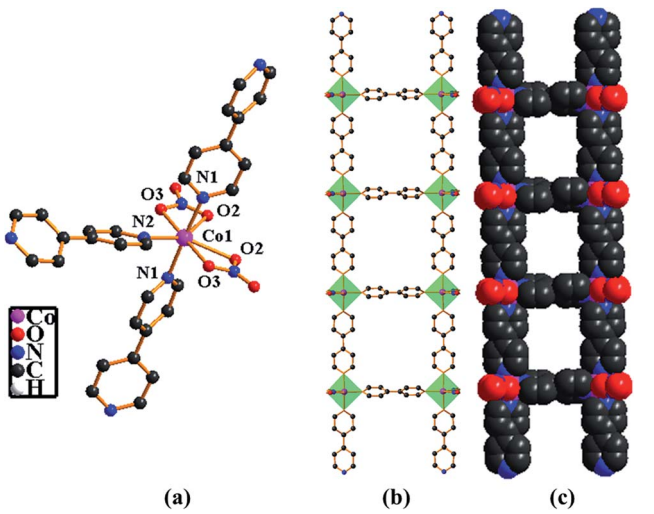

Fig. 3 Ball-stick model showing the (a) coordination environment around the Co(II) ion centre in **2** and (b) 1D ladder of **2** along the *b*-axis. (c) Space filling model of **2** along the *b*-axis. Color code: Co (magenta), O (red), N (blue), and C (dark gray) (hydrogen molecules have been omitted for clarity).

These ladder motifs subsequently stack on each other in a close-packed manner with 5.2 Å interplanar separation along the *b*-axis.

1-GCE as a supercapacitor electrode

1 was employed as the electrode material to modify the glassy carbon electrode (GCE) in the absence of any binder to fabricate the modified electrode, **1-GCE**, as mentioned above (see Experimental section). The supercapacitor properties of **1-GCE** have been studied by cyclic voltammetry (CV) and galvanostatic charge–discharge (GCD) techniques using a 1 M KOH solution (Fig. 4). The performance of **1-GCE** was also compared with the bare GCE and **2-GCE**.

Fig. 4a presents a comparison of the CV profiles of bare GCE, **1-GCE** and **2-GCE** at a scan rate of 100 mV s^{-1}, suggesting superior charge transfer and minimized internal resistance in **1**. Moreover, the CV integrated area under the curve is drastically enhanced compared to bare GCE and **2-GCE**, indicating a high charge storage efficiency of **1**. The effect of the scan rate on the CV profiles was also observed for **1-GCE**, which demonstrates that the area under the CV curve, as well as the current response, increases with an increasing scan rate (10–500 mV s^{-1}), exhibiting good capacitive behavior and charge storage characteristics (Fig. 4b). Furthermore, **1-GCE** indicates a high rate ability, as the CV profile retains a good shape even at a higher scan rate (500 mV s^{-1}) without any signal distortion. The CV profiles of **2-GCE** at different scan rates are also presented in Fig. S15a† and the current increases with increasing scan rates. However, the current responses are quite

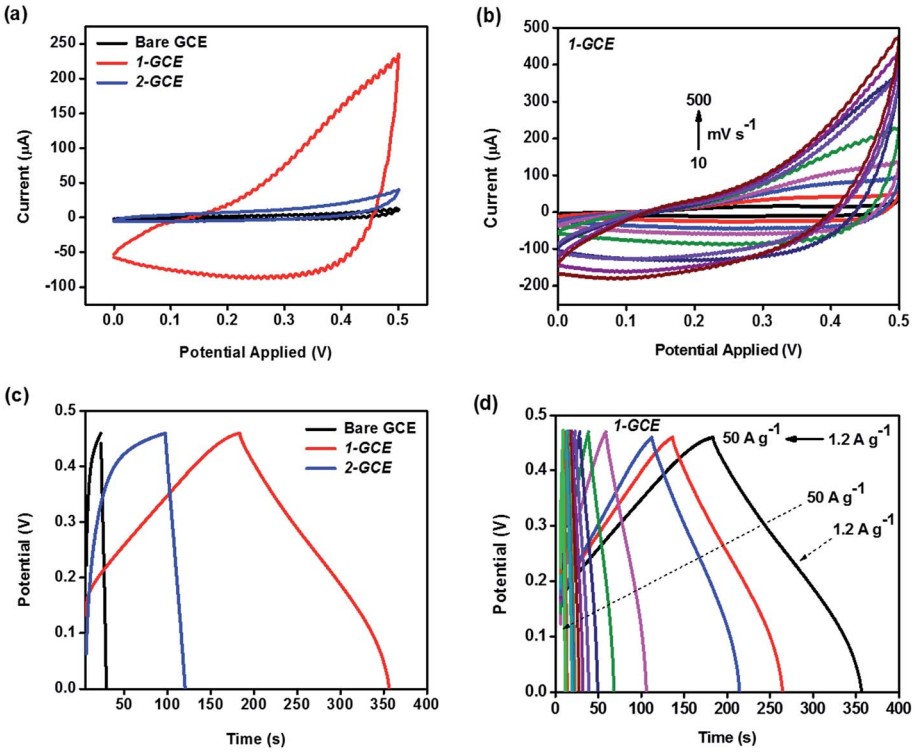

Fig. 4 (a) CV profiles for bare GCE, **1-GCE** and **2-GCE** at 100 mV s^{-1}, (b) CV profiles of **1-GCE** at varied scan rates (10–500 mV s^{-1}), (c) GCD curves for bare GCE and **1-GCE** at 1.2 A g^{-1}, and (d) GCD curves for **1-GCE** at varied current densities (1.2–50 A g^{-1}) in 1 M KOH solution.

low for **2-GCE** compared to **1-GCE**, which can be seen by comparing the *y*-axes of Fig. 4b and S15a.†

The supercapacitor performance of **1-GCE** was further investigated by studying its charge–discharge properties. A comparison of the GCD profiles of bare GCE, **1-GCE** and **2-GCE** at a current density of 1.2 A g^{-1} is presented in Fig. 4c, which shows the remarkably greater discharge time of **1** compared to the other electrodes. The observed potential drop in the bare GCE was found to be absent in **1-GCE**, which further confirms the minimized internal resistance of **1**. In addition, an undesirable voltage plateau (almost parallel to the *x*-axis), which was observed in the charging curve of **2-GCE** between 0.4–0.46 V, had almost disappeared in **1-GCE**, further signifying the potential of **1** as an energy storage material.

The GCD profiles of **1-GCE** were also recorded at different current densities (1.2–50 A g^{-1}), which demonstrate that the discharge time decreases with increasing current density, possibly due to the fact that very few electrolyte ions remain occupied at higher current densities in the inner spaces of the electrode, ultimately resulting in lower charge storage efficiencies (Fig. 4d).[30,31] A slightly changed slope can be seen in the discharge curves of **1-GCE** around 0.12 V. This may be due to the faradaic redox process happening at the electrolyte/electrode interface, which is in agreement with the CV results. However, the absence of any sharp redox peaks in the CV profiles, as well as the well-defined potential plateau in the GCD curves, suggests a lack of any obvious contribution of pseudocapacitance to the overall generated capacitance. It should be noted that in **1-GCE**, the inclined polycatenated organic framework of cobalt serves as the conductive pathway and provides efficient charge transportation,[27,29] which enhances conductivity, as observed in the CV results. GCD curves at different current densities were also recorded for **2-GCE** and asymmetrical charge–discharge curves (non-triangular) were obtained, as shown in Fig. S15b.† It can also be observed that the discharge time for **2-GCE** is much less compared to that for **1-GCE** at all current densities, which further suggests that it has a lower specific capacitance.

Comparisons of the CV and GCD profiles at 100 mV s^{-1} and 1.2 A g^{-1}, respectively, for **1-GCE** and **2-GCE** have been provided separately (Fig. S16a and b†), which clearly show the advantages of **1-GCE** over **2-GCE** for supercapacitors and highlights the presence of FcDCA, along with bpy, in **1**.

The specific capacitance at each current density was evaluated according to the equation given from the GCD curves:

$$\text{Specific capacitance} = I\mathrm{d}t/m\Delta V$$

where I is the discharge current, m represents the mass of active materials on the GCE, dt is the discharge time and ΔV is the potential window.

The calculated specific capacitances at current densities of 1.2, 1.6, 2, 4, 6, 8, 10, 20, 30 and 50 A g^{-1} are 446.8, 442.55, 438.29, 408.51, 395.74, 374.46, 361.7, 319.148, 287.23 and 265.95 F g^{-1} for **1-GCE** and 58.72, 57.87, 55.31, 46.8, 44.68, 42.55, 37.23, 29.78, 25.53 and 21.27 F g^{-1} for **2-GCE**, respectively. The good specific capacitance of **1-GCE** can be ascribed to the improved electronic conductivity and enlarged interfacial

contact between the electrode and the electrolyte interface, which shortens the ion diffusion path and improves the charge storage efficiency.[11] The presence of crystalline water also plays a pivotal role in superior supercapacitor performance. It is believed that the hydrous regions in **1** permit substantial protonic conduction, which improves the conductivity of the overall framework.[29,50]

The specific capacitances as a function of current density for **1-GCE** and **2-GCE** have been plotted in Fig. 5, which shows that the specific capacitance decreases upon increasing current density due to insufficient usage of active ionic species at higher current densities.[31] However, **1-GCE** delivers excellent rate performance by retaining ~81% of the initial capacitance up to 10 A g^{-1} and ~60% up to 50 A g^{-1}, indicating excellent ion diffusion and electron transportation for the polycatenated Co-MOF at higher current densities. However, only 36.22% of the initial capacitance was retained up to 50 A g^{-1} for **2-GCE**, demonstrating its poor rate performance.

A Ragone plot has also been demonstrated in Fig. 6a, highlighting the excellent rate performance of **1**. The obtained maximum energy and power density for **1-GCE** are 13.70 W h kg^{-1} and 11 750.99 W kg^{-1}, respectively. The cycling stability test for **1-GCE** was performed at a current density of 4 A g^{-1}, which shows that **1-GCE** retains ~88.37% of its initial specific capacitance up to 800 cycles (Fig. 6b). The inset of Fig. 6b presents the first 25 charge–discharge cycles, which shows that these cycles are reversible and confirms **1** as a potential next generation energy storage material for supercapacitors. The CV profiles of **1-GCE** before and after cycling have also been provided in Fig. S17,† which doesn't exhibit any obvious distortion, suggesting high stability of the electrode.

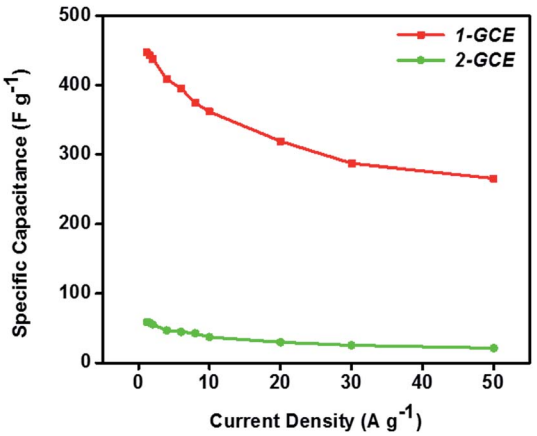

Fig. 5 Plot of specific capacitance and current density for 1-GCE and 2-GCE.

The presence of FcDCA in **1** results in an enhanced surface area with high conductivity as compared to **2** (Fig. S18 and S19, respectively†). This may be due to the electrochemical properties of ferrocene owing to the e^- withdrawing properties of the carboxylates from the cyclopentadienyl (Cp) rings, as well as the coordination bond between the carboxylate and Co ions.[48b] Therefore, it can be concluded from the above results that the presence of FcDCA, along with bpy, is highly suitable for improving supercapacitance. In addition, bpy provides structural flexibility, which is also beneficial for supercapacitor devices. This observation opens up new possibilities to design various advanced MOFs with superior supercapacitor performances. A comparison of the supercapacitor performance of **1** with similar state-of-the-art materials is summarized in Table 2. Various parameters (synthesis conditions, type of MOF, type of ligand, specific capacitance and retention of specific capacitance) have been considered to compare the performance. It can be seen that **1** (synthesized at RT) shows remarkable performance over most of the available MOFs, which were produced under harsh conditions such as high temperature. Additionally, we found only one report on a polycatenated MOF based supercapacitor,[36] with a much lower specific capacitance compared to our results. Moreover, the performance of **1** has been compared with some recently reported carbon materials/MOF composites and nanomaterials derived from MOFs (Table 3). It can be concluded from the tables that **1** is a potential energy storage material and by various modifications, further advancements can be made to achieve ultrahigh capacitance.

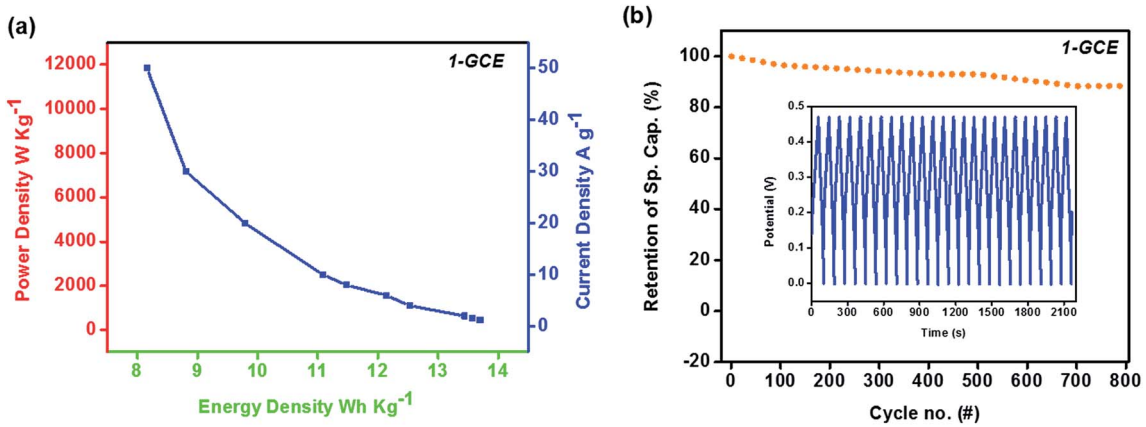

Fig. 6 (a) Ragone plot for 1-GCE and (b) cyclic stability of 1-GCE up to 800 cycles, inset shows the first 25 cycles.

Table 2 A comparison of the supercapacitor performance of the Co-MOF (**1**) synthesized in this work with some previous state-of-the-art MOFs

Material	Type of MOF	Ligand	Synthesis conditions	Specific capacitance ($F\ g^{-1}$)	Rate ($mV\ s^{-1}/A\ g^{-1}$)	Retention of specific capacitance	Reference
Cu-MOF	Layered	Hexamethylenetetramine and 2,3,5,6-tetrafluoroterephthalate	RT stirring	1274	—/1	88% after 2000 cycles	15
Co-MOF	Layered	Hexamethylenetetramine and 2,3,5,6-tetrafluoroterephthalic acid	RT stirring	2474	—/1	94.3% after 2000 cycles	20
Ni-MOF	Pillared	1,4-Diazabicyclo[2.2.2]-octane and 9,10-anthracenedicarboxylic acid	120 °C	552	—/1	>98% after 15 000 cycles	34
Zn and Cd MOFs	Polycatenated	*N*,*N*′-Bis-(4-pyridyl)phthalamide and 4,4′-biphenyldicarboxylic acid & *N*,*N*′-bis-(4-pyridyl)phthalamide and 2,5-thiophenedicarboxylic acid	120 °C	23 & 22	—/0.0025	100% after 500 cycles	36
In-MOF	Channel-type mesoporous	Benzene-[1,3,5-triyl-tris(oxy)]tribenzoic acid	120 °C	150.2	—/0.2	100% after 6000 cycles	63
Co-MOF (ZIF 67)	Sodalite-type structure	2-Methylimidazole	RT stirring	188.7	—/1	105% after 3000 cycles	64
Co-MOF film	Doctor bladed-MOF	Terephthalic acid	100 °C	206.76	—/0.6	98.5% after 1000 cycles	65
Co-MOF	Interconnected worm-like structure	*N*-Ethylperfluorooctylsulfonamide and 1,1,3,3-tetramethylguanidinium	80 °C, 16 MPa	230.5	—/0.5	95.2% after 1000 cycles	66
Co-MOF	Leaflet like structures	Terephthalic acid & 2,6-naphthalenedicarboxylic acid and 4,4′-bipyridine & 4,4-biphenyldicarboxylic acid	100 °C	131.8 & 147.3 & 179.2	10/—	77.4% after 1000 cycles	67
Co8-MOF-5	Rectangular shaped	Trimesic acid	105 °C	0.30	—/0.01	92% after 1000 cycles	68
Ni-MOF	Layered	*p*-Benzenedicarboxylic acid	120 °C	1127	—/0.5	>90% after 3000 cycles	69
$Zr\text{-}MOF_1$ $Zr\text{-}MOF_2$ $Zr\text{-}MOF_3$ $Zr\text{-}MOF_4$ (UiO-66)	3D-MOF (inorganic building brick)	Terephthalic acid	50 °C, 70 °C, 90 °C, 110 °C	1144, 811, 517, 207	5/—	57.56% after 2000 cycles	71
1	**3D inclined polycatenated**	**FcDCA and bpy**	**RT**	**446.8**	**—/1.2**	**~88.37% after 800 cycles**	**This work**

Table 3 A comparison of the specific capacitance of the Co-MOF (**1**) with some carbon materials/MOF composites, doped MOFs or nanomaterials derived from MOFs

Material	MOF	Specific capacitance ($F\ g^{-1}$)	Rate ($mV\ s^{-1}/A\ g^{-1}$)	Reference
Fe-MOF and porous carbon	Fe-MOF	39	—/0.1	28
Zn-doped Ni-MOF	Ni-MOF	1620	—/0.25	35
(Ni-MOF/CNT) composites	Ni-MOF	1765	—/0.5	70
CNTs@Mn-MOF	Mn-MOF	203.1	—/1	72
Ni-MOF-derived nickel phosphate	Ni-MOF	1627	—/1	73
Accordion like Ni-MOF	Ni-MOF	988	—/1.4	74
Worm-like mesoporous carbon (WMC)	Zn-MOF	241	—/0.1	75
Nanoporous carbon (NPC530)	Zn-MOF (MOF-5)	158	—/0.05	76
Nanoporous carbon (NPC650)	Zn-MOF (MOF-5)	222	—/0.05	76
Nanoporous carbon (NPC800)	Zn-MOF (MOF-5)	151	—/0.05	76
Nanoporous carbon (NPC900)	Zn-MOF (MOF-5)	148	—/0.05	76
Nanoporous carbon (NPC1000)	Zn-MOF (MOF-5)	149	—/0.05	76
Nanoporous carbon (NPC)	Furfuryl alcohol-MOF (FA-MOF-5)	258	—/0.25	77
Carbon material after carbonization (CZIF69a)	Zn-MOF (ZIF-69)	168	5/—	78
CZIF68a	Zn-MOF (ZIF-68)	112	5/—	78
CZIF68a	Zn-MOF (ZIF-8)	83	5/—	78
Porous carbon (C-MOF-2)	Zn-MOF (MOF-2)	170	—/1	79
Porous carbon (C-MOF-5)	Zn-MOF (MOF-5)	150	—/1	79
Porous carbon (C–Zn-BTC)	Zn-MOF (Zn-BTC)	134	—/1	79
Porous carbon (C–Zn-NDC)	Zn-MOF (Zn-NDC)	114	—/1	79
Porous carbon (C–Zn-PAA)	Zn-MOF (Zn-PAA)	110	—/1	79
Porous carbon (C–Zn-ADA)	Zn-MOF (Zn-ADA)	95	—/1	79
1	**Co-MOF**	**446.8**	**—/1.2**	**This work**

Adsorption and desorption of dyes

Inspired by the inclined polycatenated system of **1** and its unusual efficiency obtained in energy storage applications, we extended our study to the adsorption and desorption of toxic dyes, which have hazardous effects on humans as well as on aquatic systems. We have chosen two harmful contaminants (Chicago Sky Blue: CSB and Congo Red: CR), which may be present in aquatic systems during the discharge of waste from different industries. The selected dyes have a characteristic absorption peak at nearly 620 nm and 500 nm.

1 was added to a freshly prepared solution of dyes (3 mg/4 mL) at RT. As the time passed, different samples (dyes adsorbed on **1**) were collected at different time intervals. Further, these samples were centrifuged and monitored using UV-vis spectroscopy to confirm the adsorption capability of **1** towards CSB and CR. Further, the adsorption behavior of **2** was also recorded under similar conditions.

The percentage dye removal from aqueous solution was determined according to the following equation:

$$\text{Efficiency } (\%) = [(C_0 - C_t)/C_0] \times 100\%$$

where C_0 = initial concentration of dye ($mg\ L^{-1}$) and C_t = dye concentration ($mg\ L^{-1}$) at time t.

The absorption peak at 620 nm for CSB was found to notably decrease with time, and ~96.2% adsorption was observed within 15–30 min of the experiment and the solution color changed from blue to nearly colorless (Fig. 7). After 120 min, the adsorption efficiency of **1** towards CSB was calculated to be 97% and the adsorption remained the same even after 2400 min. The obtained results suggest very rapid adsorption of CSB on **1**. This observation further motivated us to explore **1** for CR dye adsorption, and ~94% adsorption was observed within 180 min (Fig. 8). A comparison of the adsorption efficiency of CSB and CR on **1** is shown in Fig. S20.†

Images of the changed color of the aqueous solutions of the dyes after the addition of **1** are presented in Fig. S21.† In addition, images were captured before (Fig. S22A†) and after the adsorption of CSB and CR on **1** (Fig. S22B and C†), which further verify the adsorption.

Unlike **1**, the adsorption efficiencies of **2** towards CSB and CR were found to be 71.7 and 11%, respectively, with a slight shift

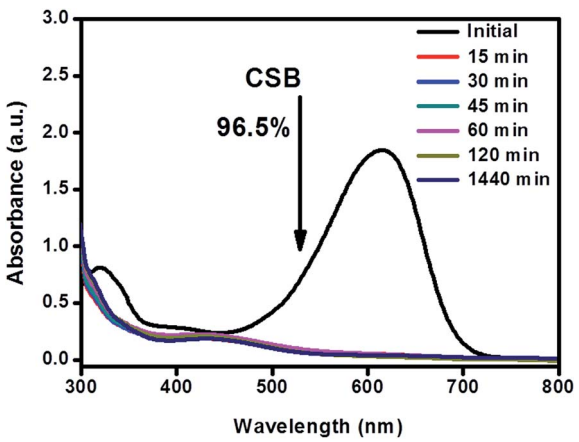

Fig. 7 UV-vis spectra of the adsorption of an aqueous solution of CSB by **1**.

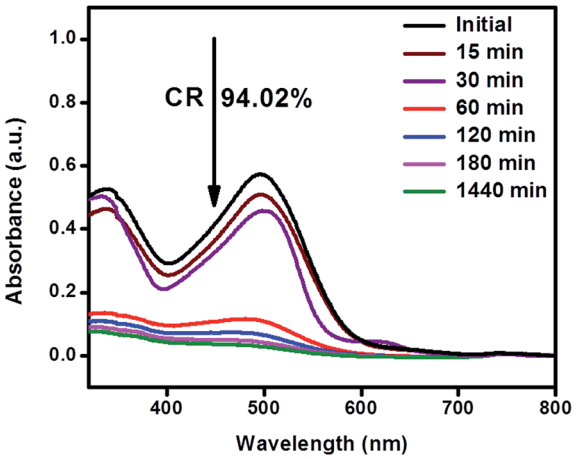

Fig. 8 UV-vis spectra of the adsorption of an aqueous solution of CR by 1.

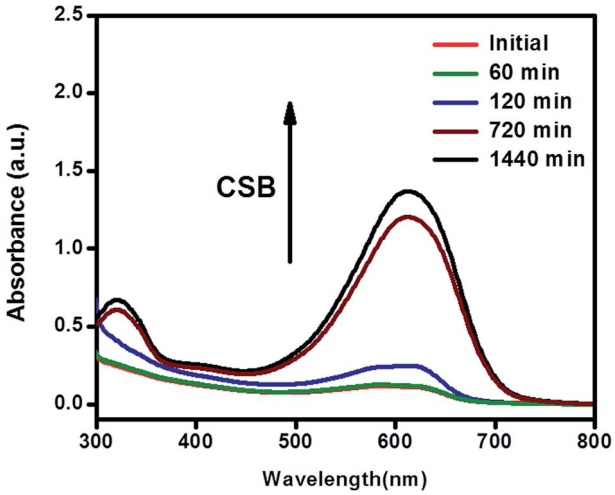

Fig. 9 UV-vis spectra of CSB released from CSB@1.

in the absorption peaks (Fig. S23 and S24†). This may be due to the partially soluble nature of **2** in water. Additionally, **1** has a higher surface area than **2**, which must be a specific reason for its enhanced dye adsorption efficiency compared to **2**. Thus, it can be concluded that **1** has advantages over **2** for use as an adsorbent in terms of stability, reusability and efficiency, and it is easily recoverable in nature due to its completely heterogeneous nature.

FTIR analysis of dyes adsorbed on 1 (CSB@1 and CR@1)

FTIR spectra of the dyes adsorbed on **1** were also recorded to confirm the appearance of related peaks of CSB adsorbed on **1** (**CSB@1**). The IR spectrum of **CSB@1** shows a strong broadened band at 3433 cm^{-1}, which is attributed to the –N–H stretching vibrations of CSB. The vibrations observed at 1252, 1103 and 1022 cm^{-1} arise due to S=O stretching and are related to CSB. It can be noted that the S=O stretching vibration of CSB is shifted to a lower region compared to **1**, which verifies the adsorption of CSB on **1**. The peaks at 800 and 622 cm^{-1} appear at lower regions compared to **1**, which further indicates the interaction of CSB with **1** (Fig. S25†).

Similarly, an IR spectrum was also recorded for CR adsorbed on **1** (**CR@1**), with similar features to those observed for **CSB@1**, which confirms the presence of the dye on the adsorbent (Fig. S26†).

Desorption/release study on 1

In addition to the adsorption of dyes, the recycling of the adsorbent is also an important parameter for practical purposes. Thus, the release of the dyes (CSB and CR) from **1** was also confirmed by performing independent experiments in methanol for 1440 min at RT. The UV-vis analysis clearly shows the gradual release of the dyes (CSB and CR) from **1** over time (Fig. 9 and 10, respectively). We believe that the % of dye in the solution can be increased by prolonging the reaction time of the desorption study. Hence, **1** can be recycled for more runs.

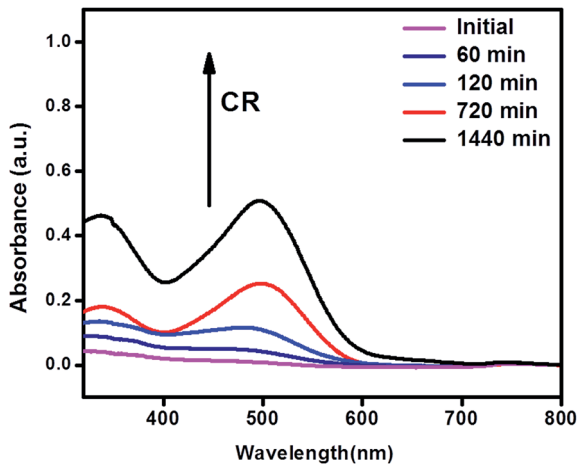

Fig. 10 UV-vis spectra of CR released from CR@1.

Effect of pH on the adsorption removal of the dye molecules (CSB and CR)

The role of pH is one of the important factors for assessing the adsorption efficiency of any material due to its influence on various factors, including the charge on the surface of the adsorbent and the properties of the dye molecule present in the aqueous system, along with the ionization/dissociation of the functional groups present on the active sites of the adsorbate molecules.[60–62]

Concerning this point, we used **1** under both acidic and basic conditions (pH = 2.0, 5.0, 7.0, 9.0 and 11.0) to perform experiments on the percentage removal of the dyes by adding the required amount of 0.1 N HCl or 0.1 N NaOH at ambient temperature (Fig. 11). The results show that the adsorption of the dyes (CSB and CR) on **1** has a pH dependent nature and the maximum adsorption of the dyes on **1** was achieved at pH 7.0. While in acidic medium, the adsorption of the dyes reaches 76% and 56% (for CSB) and 72% and 46% (for CR) at pH 5.0 and 2.0, respectively; the adsorption goes down to 40% and 21% (for

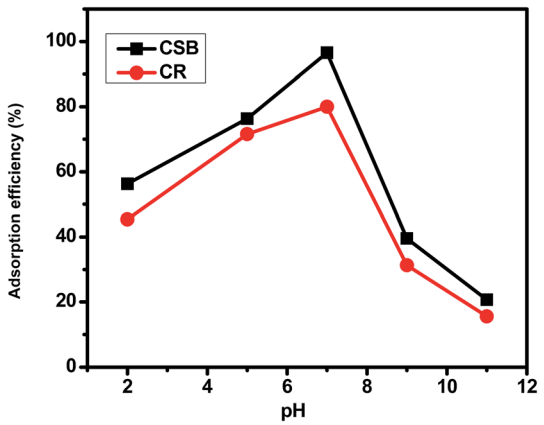

Fig. 11 Effect of pH on the adsorption efficiency of CSB and CR on **1**.

CSB) and 32% and 16% (for CR) at pH 9.0 and 11.0, respectively. The obtained results suggest that **1** also has good adsorption efficiencies for the studied dye molecules at different pH values.

The adsorption study reveals that **1** retains over ~90% of its original adsorption efficiency even after 3 successive runs under the same experimental conditions, as shown in Fig. S27.† Hence, **1** can be recycled easily.

Conclusions

We have successfully designed and synthesized a new 3D inclined polycatenated Co-MOF, $\{[Co_4(FcDCA)_4(bpy)_4(H_2O)_6]\cdot 11H_2O\}_n$ (**1**), by a facile mixed-ligand strategy. The introduction of highly electro-active ferrocene based ligands not only provides structural integrity and flexibility to the framework, but also improves the electrochemical performance. The applicability of **1** was explored by studying its supercapacitor properties. The charge–discharge study reveals its high charge storage efficiency (446.8 F g^{-1} at a current density of 1.2 A g^{-1}) with an excellent cycle life and a remarkable rate performance, which is so far the best supercapacitance of any polycatenated MOF. The supercapacitor performance of **2** was also evaluated for comparison, and showed considerably less supercapacitance than **1**. Therefore, the good supercapacitor performance of **1** was assigned to the presence of FcDCA, which significantly enhanced the conduction due to the presence of a large number of lattice water molecules. The results indicate the future potential of the newly designed Co-MOF, and suggest that inclined polycatenated MOFs could be alternative next generation energy storage electrode materials. Additionally, the adsorption behaviour of **1** for CSB and CR dyes was also studied, revealing excellent percentage removal efficiencies (97% and 94% for CSB and CR, respectively). Moreover, **1** can be recycled for more runs and has the advantage of adsorbing dyes in acidic as well as basic media. These results show that **1** has the ability to rectify the problem of dye contaminated aquatic systems.

Conflict of interest

There are no conflicts of interest to declare.

Acknowledgements

We sincerely acknowledge Sophisticated Instrumentation Centre (SIC), IIT Indore for all the characterization facilities. R. R. thanks DST for Inspire fellowship. M. S. and A. M. thank MHRD, New Delhi, India for providing research fellowships. We thank Prof. Dr. Matthias Tamm, Institut für Anorganische und Analytische Chemie, Technische Universität Braunschweig, for providing the 1,1′-ferrocene dicarboxylic acid. We gratefully acknowledge Dr. Pankaj Sagdeo and Mr. Md Kamal Warshi, IIT Indore for helping in conductivity measurements and Prof. Davide M. Proserpio, University of Milan for his help in understanding topology of **1**. S. M. M. thanks SERB-DST (Project No. EMR/2016/001113), New Delhi, India for financial support.

References

1 J. A. Mason, M. Veenstra and J. R. Long, *Chem. Sci.*, 2014, **5**, 32–51.
2 N. L. Rosi, J. Eckert, M. Eddaoudi, D. T. Vodak, J. Kim, M. O'Keeffe and O. M. Yaghi, *Science*, 2003, **300**, 1127–1129.
3 M. Eddaoudi, J. Kim, N. Rosi, D. Vodak, J. Wachter, M. O'Keeffe and O. M. Yaghi, *Science*, 2002, **295**, 469–472.
4 S. Parshamoni, S. Sanda, H. S. Jena and S. Konar, *Dalton Trans.*, 2014, **43**, 7191–7199.
5 B. Gómez-Lor, E. Gutiérrez-Puebla, M. Iglesias, M. A. Monge, C. Ruiz-Valero and N. Snejko, *Chem. Mater.*, 2005, **17**, 2568–2573.
6 Z. Hasan and S. H. Jhung, *ACS Appl. Mater. Interfaces*, 2015, **7**, 10429–10435.
7 N. C. Thacker, Z. Lin, T. Zhang, J. C. Gilhula, C. W. Abney and W. Lin, *J. Am. Chem. Soc.*, 2016, **138**, 3501–3509.
8 S. Sanda, S. Parshamoni, S. Biswas and S. Konar, *Chem. Commun.*, 2015, **51**, 6576–6579.
9 A. A. Tehrani, L. Esrafili, S. Abedi, A. Morsali, L. Carlucci, D. M. Proserpio, J. Wang, P. C. Junk and T. Liu, *Inorg. Chem.*, 2017, **56**, 1446–1454.
10 D. K. Maity, A. Halder, G. Pahari, F. Haque and D. Ghoshal, *Inorg. Chem.*, 2017, **56**, 713–716.
11 M. Saraf, R. Rajak and S. M. Mobin, *J. Mater. Chem. A*, 2016, **4**, 16432–16445.
12 W. A. Maza, A. J. Haring, S. R. Ahrenholtz, C. C. Epley, S. Y. Lin and A. J. Morris, *Chem. Sci.*, 2016, **7**, 719–727.
13 F. Zou, X. Hu, Z. Li, L. Qie, C. Hu, R. Zeng, Y. Jiang and Y. Huang, *Adv. Mater.*, 2014, **26**, 6622–6628.
14 G. Fang, J. Zhou, C. Liang, A. Pan, C. Zhang, Y. Tang, X. Tan, J. Liu and S. Liang, *Nano Energy*, 2016, **26**, 57–65.
15 Q. Liu, X. Liu, C. Shi, Y. Zhang, X. Feng, M.-L. Cheng, S. Su and J. Gu, *Dalton Trans.*, 2015, **44**, 19175–19184.
16 T. Song, J. Yu, Y. Cui, Y. Yang and G. Qian, *Dalton Trans.*, 2016, **45**, 4218–4223.
17 J. R. Miller and P. Simon, *Science*, 2008, **321**, 651–652.
18 P. Simon and Y. Gogotsi, *Nat. Mater.*, 2008, **7**, 845–854.
19 L. Wang, Y. Han, X. Feng, J. Zhou, P. Qi and B. Wang, *Coord. Chem. Rev.*, 2016, **307**, 361–381.
20 X. Liu, C. Shi, C. Zhai, M. Cheng, Q. Liu and G. Wang, *ACSAppl. Mater. Interfaces*, 2016, **8**, 4585–4591.

21 W. Xia, C. Qu, Z. Liang, B. Zhao, S. Dai, B. Qiu, Y. Jiao, Q. Zhang, X. Huang, W. Guo, D. Dang, R. Zou, D. Xia, Q. Xu and M. Liu, *Nano Lett.*, 2017, **17**, 2788–2795.
22 C. Qu, B. Zhao, Y. Jiao, D. Chen, S. Dai, B. M. deglee, Y. Chen, K. S. Walton, R. Zou and M. Liu, *ACS Energy Lett.*, 2017, **2**, 1263–1269.
23 S. Liu, J. Zhou, Z. Cai, G. Fang, Y. Cai, A. Pan and S. Liang, *J. Mater. Chem. A*, 2016, **4**, 17838–17847.
24 R. R. Salunkhe, Y. V. Kaneti, J. Kim, J. H. Kim and Y. Yamauchi, *Acc. Chem. Res.*, 2016, **49**, 2796–2806.
25 G. Fang, J. Zhou, Y. Cai, S. Liu, X. Tan, A. Pan and S. Liang, *J. Mater. Chem. A*, 2017, **5**, 13983–13993.
26 G. Wang, L. Zhang and J. Zhang, *Chem. Soc. Rev.*, 2012, **41**, 797–828.
27 C. Wang, C. Liu, J. Li, X. Sun, J. Shen, W. Han and L. Wang, *Chem. Commun.*, 2017, **53**, 1751–1754.
28 N. Campagnol, R. Romero-Vara, W. Deleu, L. Stappers, K. Binnemans, D. E. Devos and J. Fransaer, *ChemElectroChem*, 2014, **1**, 1182–1188.
29 Y. Jiao, J. Pei, D. Chen, C. Yan, Y. Hu, Q. Zhang and G. Chen, *J. Mater. Chem. A*, 2017, **5**, 1094–1102.
30 M. Saraf, K. Natarajan and S. M. Mobin, *RSC Adv.*, 2017, **7**, 309–317.
31 M. Saraf, R. A. Dar, K. Natarajan, A. K. Srivastava and S. M. Mobin, *ChemistrySelect*, 2016, **1**, 2826–2833.
32 G. Zhu, C. Xi, M. Shen, C. Bao and J. Zhu, *ACS Appl. Mater. Interfaces*, 2014, **6**, 17208–17214.
33 J. Yang, Z. Ma, W. Gao and M. Wei, *Chem.–Eur. J.*, 2016, **22**, 1–7.
34 C. Qu, Y. Jiao, B. Zhao, D. Chen, R. Zou, K. S. Walton and M. Liu, *Nano Energy*, 2016, **26**, 66–73.
35 J. Yang, C. Zheng, P. Xiong, Y. Li and M. Wei, *J. Mater. Chem. A*, 2014, **2**, 19005–19010.
36 Y. Gong, J. Li, P.-G. Jiang, Q.-F. Li and J.-H. Lin, *Dalton Trans.*, 2013, **42**, 1603–1611.
37 Y. Shen, C.-C. Fan, Y.-Z. Wei, J. Du, H.-B. Zhu and Y. Zhao, *Dalton Trans.*, 2016, **45**, 10909–10915.
38 D. M. Chen, W. Shi and P. Cheng, *Chem. Commun.*, 2015, **51**, 370–372.
39 R. Zhao, Y. Wang, X. Li, B. L. Sun and C. Wang, *ACS Appl. Mater. Interfaces*, 2015, **7**, 26649–26657.
40 A. Mohammad, K. Kapoor and S. M. Mobin, *ChemistrySelect*, 2016, **1**, 3483–3490.
41 Y. Song, R.-Q. Fan, K. Xing, X. Du, T. Su, P. Wang and Y.-L. Yang, *Cryst. Growth Des.*, 2017, **17**, 2549–2559.
42 K. M. Choi, H. M. Jeong, J. H. Park, Y.-B. Zhang, J. K. Kang and O. M. Yaghi, *ACS Nano*, 2014, **8**, 7451–7457.
43 H. Chen, D. Xiao, J. He, Z. Li, G. Zhang, D. Sun, R. Yuan, E. Wang and Q.-L. Luo, *CrystEngComm*, 2011, **13**, 4988–5000.
44 D.-S. Li, P. Zhang, J. Zhao, Z.-F. Fang, M. Du, K. Zou and Y.-Q. Mu, *Cryst. Growth Des.*, 2012, **12**, 1697–1702.
45 L. Carlucci, G. Ciani and D. M. Proserpio, *Coord. Chem. Rev.*, 2003, **246**, 247–289.
46 T.-T. Wu, W. Hsu, X.-K. Yang, H.-Y. He and J.-D. Chen, *CrystEngComm*, 2015, **17**, 916–924.
47 L. Carlucci, G. Ciani, D. M. Proserpio, T. G. Mitina and V. A. Blatov, *Chem. Rev.*, 2014, **114**, 7557–7580.
48 (*a*) X. Meng, W. Cheng, L. Mi, M. Tang and H. Hou, *Inorg. Chem. Commun.*, 2006, **9**, 662–665; (*b*) K. Hirai, H. Uehara, S. Kitagawa and S. Furukawa, *Dalton Trans.*, 2012, **41**, 3924–3927.
49 G. M. Sheldrick, *Acta Crystallogr., Sect. A: Found. Crystallogr.*, 2008, **64**, 112–122.
50 L. J. Farrugia, *J. Appl. Crystallogr.*, 1999, **32**, 837.
51 M. Felloni, A. J. Blake, N. R. Champness, P. Hubberstey, C. Wilson and M. Schroder, *J. Supramol. Chem.*, 2002, **2**, 163–174.
52 L. Carlucci, G. Ciani and D. M. Proserpio, *J. Chem. Soc., Dalton Trans.*, 1999, **11**, 1799–1804.
53 P. Losier and M. J. Zaworotko, *Angew. Chem., Int. Ed. Engl.*, 1996, **35**, 2779–2782.
54 K. M. Sonnek, L. K. Streicher, O. P. Lamp, A. Ellern and C. L. Weeks, *Inorg. Chim. Acta*, 2014, **418**, 73–83.
55 H. Erer, O. Z. Yeşilel, M. Arıcı, S. Keskin and O. Büyükgüngör, *J. Solid State Chem.*, 2014, **210**, 261–266.
56 R. Sen, D. Saha, D. Mal, P. Brandão, G. Rogez and Z. Lin, *Eur. J. Inorg. Chem.*, 2013, **2013**, 3076–3081.
57 X.-C. Wang, Q. Yang, J. Li, H.-L. Xu, H. Yuan and D.-R. Xiao, *Inorg. Chim. Acta*, 2016, **451**, 123–128.
58 J. Fan, H.-F. Zhu, T. Okamura, W.-Y. Sun, W.-X. Tang and N. Ueyama, *Inorg. Chem.*, 2003, **42**, 158–162.
59 X. Kuang, X. Wu, R. Yu, P. J. Donahue, J. Huang and C.-Z. Lu, *Nat. Chem.*, 2010, **2**, 461–465.
60 T. K. Mahto, S. Chandra, C. Haldar and S. K. Sahu, *RSC Adv.*, 2015, **5**, 47909–47919.
61 L. Ai, C. Zhang and Z. Chen, *J. Hazard. Mater.*, 2011, **192**, 1515–1524.
62 M. Anbia, S. A. Hariri and S. Ashrafizadeh, *Appl. Surf. Sci.*, 2010, **256**, 3228–3233.
63 M. Du, M. Chen, X.-G. Yang, J. Wen, X. Wang, S.-M. Fang and C.-S. Liu, *J. Mater. Chem A*, 2014, **2**, 9828–9834.
64 D. Zhang, H. Shi, R. Zhang, Z. Zhang, N. Wang, J. Li, B. Yuan, H. Bai and J. Zhang, *RSC Adv.*, 2015, **5**, 58772–58776.
65 D. Y. Lee, S. J. Yoon, N. K. Shrestha, S. H. Lee, H. Ahn and S. H. Han, *Microporous Mesoporous Mater.*, 2012, **153**, 163–165.
66 H. Yu, D. Xu and Q. Xu, *Chem. Commun.*, 2015, **51**, 13197–13200.
67 D. Y. Lee, D. V. Shinde, E. K. Kim, W. Lee, I. W. Oh, N. K. Shrestha, J. K. Lee and S. H. Han, *Microporous Mesoporous Mater.*, 2013, **171**, 53–57.
68 R. Díaz, M. G. Orcajo, J. A. Botas, G. Calleja and J. Palma, *Mater. Lett.*, 2012, **68**, 126–128.
69 J. Yang, P. X. Xiong, C. Zheng, H. Qiu and M. D. Wei, *J. Mater. Chem. A*, 2014, **2**, 16640–16644.
70 P. Wen, P. Gong, J. Sun, J. Wang and S. Yang, *J. Mater. Chem. A*, 2015, **3**, 13874–13883.
71 Y. Tan, W. Zhang, Y. Gao, J. Wu and B. Tang, *RSC Adv.*, 2015, **5**, 17601–17605.
72 Y. Zhang, B. Lin, Y. Sun, X. Zhang, H. Yang and J. Wang, *RSC Adv.*, 2015, **5**, 58100–58106.
73 R. Bendi, V. Kumar, V. Bhavanasi, K. Parida and P. S. Lee, *Adv. Energy Mater.*, 2016, **6**, 1501833.

74 Y. Yan, P. Gu, S. Zheng, M. Zheng, H. Pang and H. Xue, *J. Mater. Chem. A*, 2016, **4**, 19078–19085.
75 D. Yuan, J. Chen, S. Tan, N. Xia and Y. Liu, *Electrochem. Commun.*, 2009, **11**, 1191–1194.
76 B. Liu, H. Shioyama, H. Jiang, X. Zhang and Q. Xu, *Carbon*, 2010, **48**, 456–463.
77 B. Liu, H. Shioyama, T. Akita and Q. Xu, *J. Am. Chem. Soc.*, 2008, **130**, 5390–5391.
78 Q. Wang, W. Xia, W. Guo, L. An, D. Xia and R. Zou, *Chem.–Asian J.*, 2013, **8**, 1879–1885.
79 H. B. Aiyappa, P. Pachfule, R. Banerjee and S. Kurungot, *Cryst. Growth Des.*, 2013, **13**, 4195–4199.